Обзор ArXiv/astro-ph, 25 мая-5 июня 2020 года

От Сильченко О.К.

ArXiv: 2005.11709

PHANGS CO kinematics: disk orientations and rotation curves at 150 pc resolution

Philipp Lang,[1] Sharon E. Meidt,[2] Erik Rosolowsky,[3] Joseph Nofech,[3] Eva Schinnerer,[1] Adam K. Leroy,[4] Eric Emsellem,[5,6] Ismael Pessa,[1] Simon C. O. Glover,[7] Brent Groves,[8,9] Annie Hughes,[10,11] J. M. Diederik Kruijssen,[12] Miguel Querejeta,[13] Andreas Schruba,[14] Frank Bigiel,[15] Guillermo A. Blanc,[16,17] Mélanie Chevance,[12] Dario Colombo,[18] Christopher Faesi,[1] Jonathan D. Henshaw,[1] Cinthya N. Herrera,[19] Daizhong Liu,[1] Jérôme Pety,[19,20] Johannes Puschnig,[15] Toshiki Saito,[1] Jiayi Sun,[4] and Antonio Usero[13]

[1] *Max-Planck-Institut für Astronomie, Königstuhl 17 D-69117 Heidelberg, Germany*

[2] *Sterrenkundig Observatorium, Universiteit Gent, Krijgslaan 281 S9, B-9000 Gent, Belgium*

[3] *Department of Physics, University of Alberta, Edmonton, AB, Canada*

[4] *Department of Astronomy, The Ohio State University, 140 West 18th Avenue, Columbus, Ohio 43210, USA*

[5] *European Southern Observatory, Karl-Schwarzschild Straße 2, D-85748 Garching bei München, Germany*

[6] *Univ Lyon, Univ Lyon1, ENS de Lyon, CNRS, Centre de Recherche Astrophysique de Lyon UMR5574, F-69230 Saint-Genis-Laval France*

[7] *Institüt für Theoretische Astrophysik, Zentrum für Astronomie der Universität Heidelberg, Albert-Ueberle-Strasse 2, 69120 Heidelberg, Germany*

[8] *Research School of Astronomy and Astrophysics, Australian National University, Canberra, ACT 2611, Australia*

[9] *International Centre for Radio Astronomy Research, The University of Western Australia, Crawley, WA 6009 Australia*

[10] *Université de Toulouse, UPS-OMP, 31028 Toulouse, France*

[11] *CNRS, IRAP, Av. du Colonel Roche BP 44346, 31028 Toulouse cedex 4, France*

[12] *Astronomisches Rechen-Institut, Zentrum für Astronomie der Universität Heidelberg, Mönchhofstraße 12-14, 69120 Heidelberg, Germany*

[13] *Observatorio Astronómico Nacional (IGN), C/Alfonso XII 3, Madrid E-28014, Spain*

[14] *Max-Planck-Institut für Extraterrestrische Physik, Giessenbachstraße 1, D-85748 Garching bei München, Germany*

[15] *Argelander-Institut für Astronomie, Universität Bonn, Auf dem Hügel 71, 53121 Bonn, Germany*

[16] *The Observatories of the Carnegie Institution for Science, 813 Santa Barbara St., Pasadena, CA, 91101*

[17] *Departamento de Astronomía, Universidad de Chile, Camino del Observatorio 1515, Las Condes, Santiago, Chile*

[18] *Max-Planck-Institut für Radioastronomie, Auf dem Hügel 9, D-53121 Bonn, Germany*

[19] *Institut de Radioastronomie Millimétrique, 300 rue de la Piscine, 38406 Saint-Martin-d'Hères Cedex*

[20] *Sorbonne Université, Observatoire de Paris, Université PSL, CNRS, LERMA, 75014, Paris, France*

Выборка

In this paper, we present global disk orientations and rotation curves from $\sim 1''$ PHANGS-ALMA[1] CO data extending on average out to $\sim 0.7\,R_{25}$ for 67 local star-forming galaxies. This is the largest such compilation of CO rotation curves to date (c.f., Sofue & Rubin 2001)

D<17 Mpc, i<75deg, logM_*>9.75

Выборка

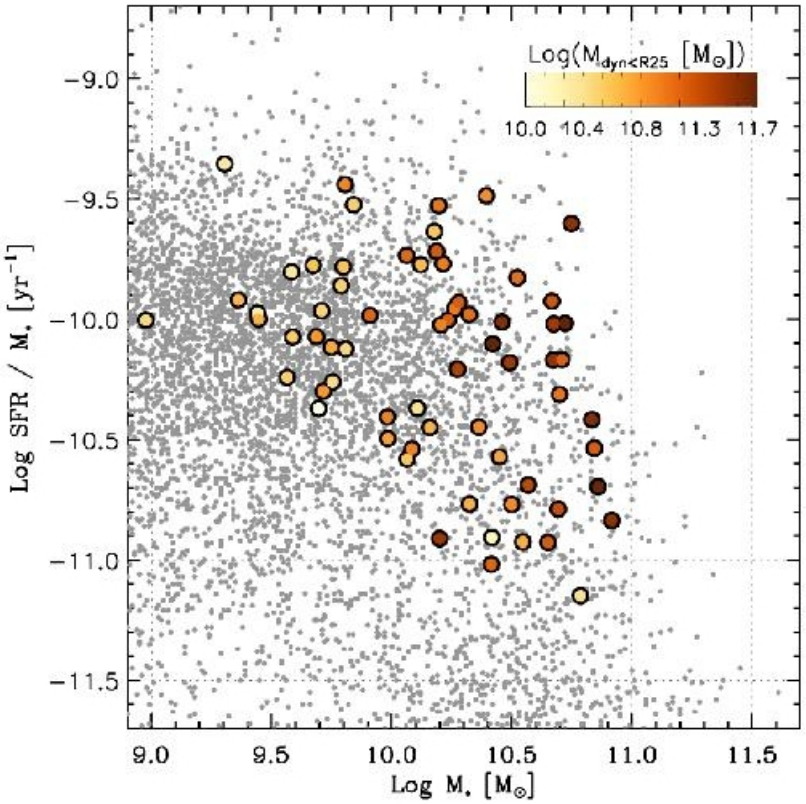

Figure 1. The subset of the PHANGS-ALMA sample used for this paper (colored symbols) in the $M_\star$−sSFR plane. The color-coding indicates the total dynamical mass within R_{25} ($M_{\rm dyn,R_{25}}$, see Section 4.4.3). The underlying population of star-forming galaxies taken from Leroy et al. (2019) is shown as gray symbols (see text for details). Our kinematic sample spans a large range of stellar masses, SFRs, and ratios of stellar-to-total dynamical masses, while well sampling the

Выборка

Table 1. Basic properties of the kinematic PHANGS sample

ID	RA[1] [deg]	DEC[1] [deg]	Distance [Mpc]	V_{sys}[2] [km s^{-1}]	ϕ_{phot}[3] [deg]	i_{phot}[4] [deg]	f_{CO}[5] [arcsec]	$\frac{R_{min}}{R_{CO,max}}$	$\frac{R_{CO,max}}{R_{25}}$
IC 1954	52.97071	−51.90486	13.2	1062.9	61.0	57.7	0.46	0.09	0.84
IC 5273	344.86118	−37.70284	14.7	1293.9	229.0	44.3	0.27	0.22	0.97
NGC 0628	24.17385	15.78364	9.8	658.5	0.1	18.9	0.29	0.00	0.55
NGC 0685	26.92845	−52.70198	16.0	1359.7	99.2	38.6	0.21	0.25	0.87
NGC 1087	41.60392	−0.49873	14.4	1522.7	1.4	51.4	0.36	0.20	0.94
NGC 1097	41.57896	−30.27467	14.2	1263.4	126.5	48.6	0.25	0.32	0.57
NGC 1300	49.92081	−19.41111	16.1	1578.2	286.1	31.8	0.30	0.08	0.67
NGC 1317	50.68464	−37.10379	19.0	1948.5	300.3	25.0	0.48	0.19	0.35
NGC 1365	53.40152	−36.14040	18.1	1638.3	210.7	55.4	0.34	0.52	0.49
NGC 1385	54.36001	−24.50016	22.7	1497.3	172.3	49.7	0.34	0.00	0.72
NGC 1433	55.50619	−47.22194	16.8	1075.1	204.3	28.6	0.09	0.05	0.75
NGC 1511	59.90246	−67.63192	15.6	1334.9	304.0	71.1	0.31	0.20	0.95
NGC 1512	60.97357	−43.34872	16.8	897.7	254.5	42.5	0.12	0.02	0.45
NGC 1546	63.65122	−56.03690	18.0	1252.9	147.4	67.4	0.46	0.00	0.72
NGC 1559	64.40238	−62.78341	19.8	1295.4	245.1	54.0	0.31	0.09	1.00
NGC 1566	65.00159	−54.93801	18.0	1501.8	300.9	30.4	0.26	0.27	0.61
NGC 1672	71.42704	−59.24736	11.9	1338.8	148.5	23.7	0.39	0.48	0.83
NGC 1792	76.30969	−37.98856	13.8	1210.6	316.1	60.7	0.34	0.00	0.81
NGC 1809	75.52066	−69.54794	15.0	1203.6	144.8	80.5	0.30	0.00	0.57
NGC 2090	85.75787	−34.25060	11.8	922.1	196.5	71.7	0.44	0.00	0.53
NGC 2283	101.42357	−18.21080	13.4	843.6	0.1	44.2	0.38	0.14	1.05
NGC 2566	124.60003	−25.49952	23.7	1637.9	235.6	48.5	0.15	0.46	1.02
NGC 2775	137.58396	7.03897	17.0	1354.1	153.5	34.2	0.30	0.00	0.58
NGC 2835	139.47044	−22.35468	10.1	880.5	0.3	36.4	0.07	0.23	0.48
NGC 2903	143.04212	21.50081	8.5	555.3	199.6	63.5	0.38	0.25	0.75
NGC 2997	146.41164	−31.19109	11.3	1086.9	96.6	54.3	0.42	0.06	0.62
NGC 3059	147.53400	−73.93219	19.8	1228.0	−5.0	21.2	0.30	0.22	0.77
NGC 3137	152.28116	−29.08430	14.9	1108.1	3.9	47.2	0.30	0.00	0.53
NGC 3351	160.99084	11.70367	10.0	778.0	193.4	45.1	0.25	0.41	0.58
NGC 3507	165.85373	18.13552	20.9	975.6	80.1	27.5	0.27	0.34	0.85
NGC 3511	165.84821	−23.08871	9.9	1105.4	258.4	72.1	0.30	0.11	0.94
NGC 3521	166.45240	−0.03599	11.2	800.9	342.3	66.2	0.44	0.00	0.69
NGC 3596	168.77081	14.78797	10.1	1102.4	103.2	16.9	0.27	0.00	0.66
NGC 3621	169.56792	−32.81266	6.6	730.1	341.2	65.5	0.34	0.00	0.83
NGC 3626	170.01568	18.35484	20.0	1470.5	163.2	46.6	0.40	0.88	0.20
NGC 3627	170.06252	12.99159	10.6	720.9	166.2	55.7	0.40	0.37	0.58
NGC 4207	183.97081	9.58193	16.8	608.6	121.3	70.5	0.27	0.00	0.89
NGC 4254	184.70680	14.41641	16.8	2407.9	76.6	35.2	0.33	0.00	1.13

Table 1 *(continued)*

ID	RA[1] [deg]	DEC[1] [deg]	Distance [Mpc]	V_{sys}[2] [km s^{-1}]	ϕ_{phot}[3] [deg]	i_{phot}[4] [deg]	f_{CO}[5] [arcsec]	$\frac{R_{min}}{R_{CO,max}}$	$\frac{R_{CO,max}}{R_{25}}$
NGC 4293	185.30316	18.38257	16.0	901.6	64.0	65.0	0.16	1.32	0.32
NGC 4298	185.36951	14.60613	16.8	1128.4	311.1	56.4	0.53	0.00	1.21
NGC 4303	185.47888	4.47374	17.6	1566.9	323.6	24.2	0.56	0.36	0.49
NGC 4321	185.72886	15.82230	15.2	1571.9	158.2	33.2	0.30	0.04	1.03
NGC 4457	187.24202	3.57082	15.6	884.9	66.4	17.4	0.48	0.78	0.50
NGC 4496a	187.91358	3.93982	14.9	1730.4	62.4	59.1	0.12	0.29	0.80
NGC 4535	188.58459	8.19787	15.8	1952.1	202.8	22.4	0.33	0.28	0.54
NGC 4536	188.61278	2.18824	15.2	1807.3	305.5	67.7	0.25	0.19	0.84
NGC 4540	188.71199	15.55172	16.8	1284.1	90.0	11.8	0.34	0.41	0.68
NGC 4548	188.86024	14.49633	16.2	481.5	140.2	38.3	0.25	0.52	0.60
NGC 4569	189.20759	13.16287	16.8	−210.5	24.8	69.7	0.33	0.61	0.58
NGC 4571	189.23392	14.21733	14.9	335.7	214.1	14.1	0.28	0.00	0.74
NGC 4579	189.43138	11.81832	16.8	1516.8	92.1	41.3	0.49	0.37	0.72
NGC 4654	190.99575	13.12872	16.8	1043.4	123.7	58.6	0.37	0.22	0.91
NGC 4689	191.93990	13.76272	16.8	1608.4	163.7	35.3	0.41	0.00	0.70
NGC 4781	193.39016	−10.53712	15.3	1262.3	280.8	61.5	0.33	0.18	0.92
NGC 4826	194.18184	21.68308	4.4	407.6	295.9	58.2	0.22	0.00	0.98
NGC 4941	196.05461	−5.55154	14.0	1111.2	203.5	39.4	0.46	0.00	0.83
NGC 4951	196.36212	−6.45582	12.0	1177.6	91.5	76.1	0.24	0.00	0.83
NGC 5042	198.87020	−23.98388	12.6	1389.1	195.9	57.4	0.28	0.30	0.53
NGC 5068	199.72808	−21.03874	5.2	671.2	340.1	27.0	0.05	0.17	0.94
NGC 5134	201.32726	−21.13419	18.5	1755.7	300.0	4.9	0.24	0.79	0.70
NGC 5248	204.38386	8.88519	12.7	1152.3	103.9	47.8	0.25	0.00	0.98
NGC 5530	214.61380	−43.38826	11.8	1193.1	306.5	66.5	0.30	0.00	0.70
NGC 5643	218.16991	−44.17463	11.8	1190.0	323.6	29.0	0.41	0.45	0.76
NGC 6300	259.24780	−62.82055	13.1	1108.7	118.6	53.2	0.32	0.16	0.79
NGC 6744	287.44268	−63.85734	9.5	851.4	15.4	53.5	0.14	0.26	0.53
NGC 7456	345.34306	−39.56841	7.9	1200.7	22.9	78.2	0.20	0.00	0.69
NGC 7496	347.44705	−43.42765	18.7	1650.3	213.2	9.0	0.37	0.44	0.80

NOTE—1: Adopted photometric galaxy center; 2: prior of systemic velocity; 3: prior of photometric disk position angle; 4: prior of photometric disk inclination; 5: spatial CO covering fraction.

Пример анализа

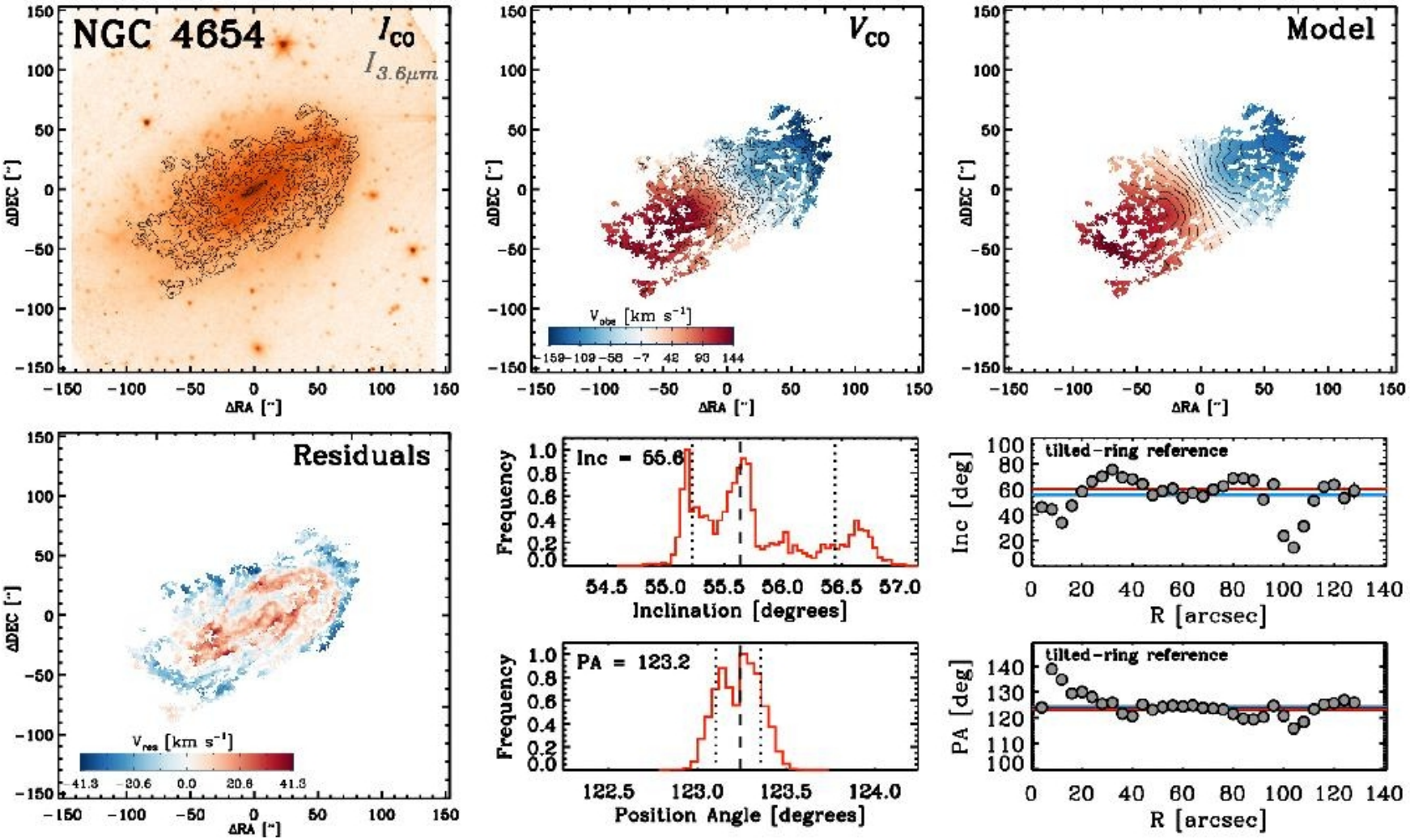

Сравнение ориентации газового и звездного диска (S4G)

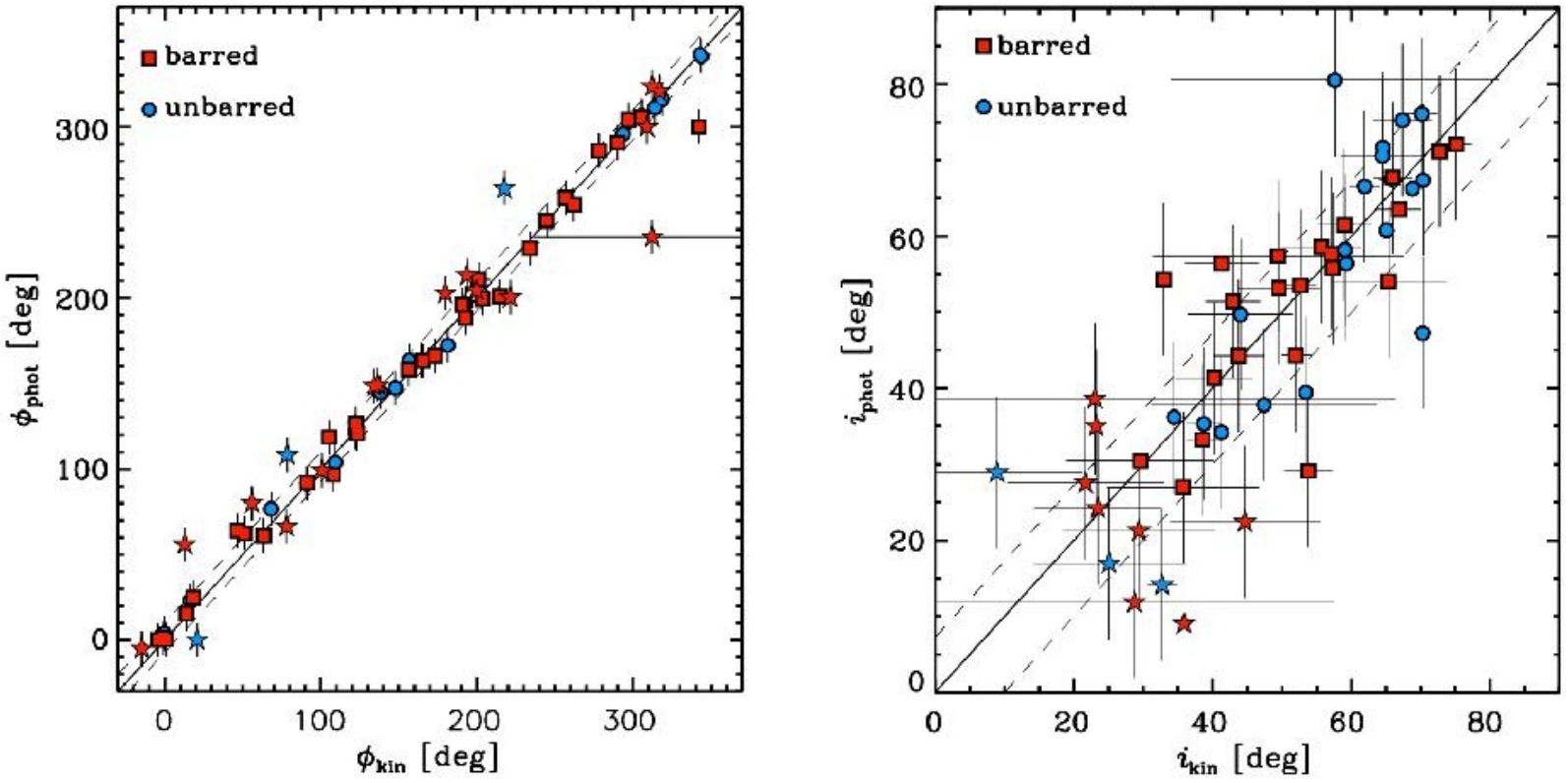

Figure 5. Best-fit position angles ϕ and inclinations i determined from kinematics versus photometry. We split our sample in barred (red) and unbarred (blue) systems to highlight the impact of bars on measured galaxy orientation. In addition, nearly face-on systems with either i_{kin} or $i_{phot} < 25$ degrees are marked with a different symbol. The right panel only includes the subset of 52 galaxies with reliable i_{kin} measurement (see Section 4.2). The shown error bars represent the uncertainties listed in Table 2, and are derived from our jackknife analysis. Solid and dashed lines represent a one-to-one correlation and the scatter in the relations, respectively (see Table 3 for tabulated values).

Примеры кривых вращения

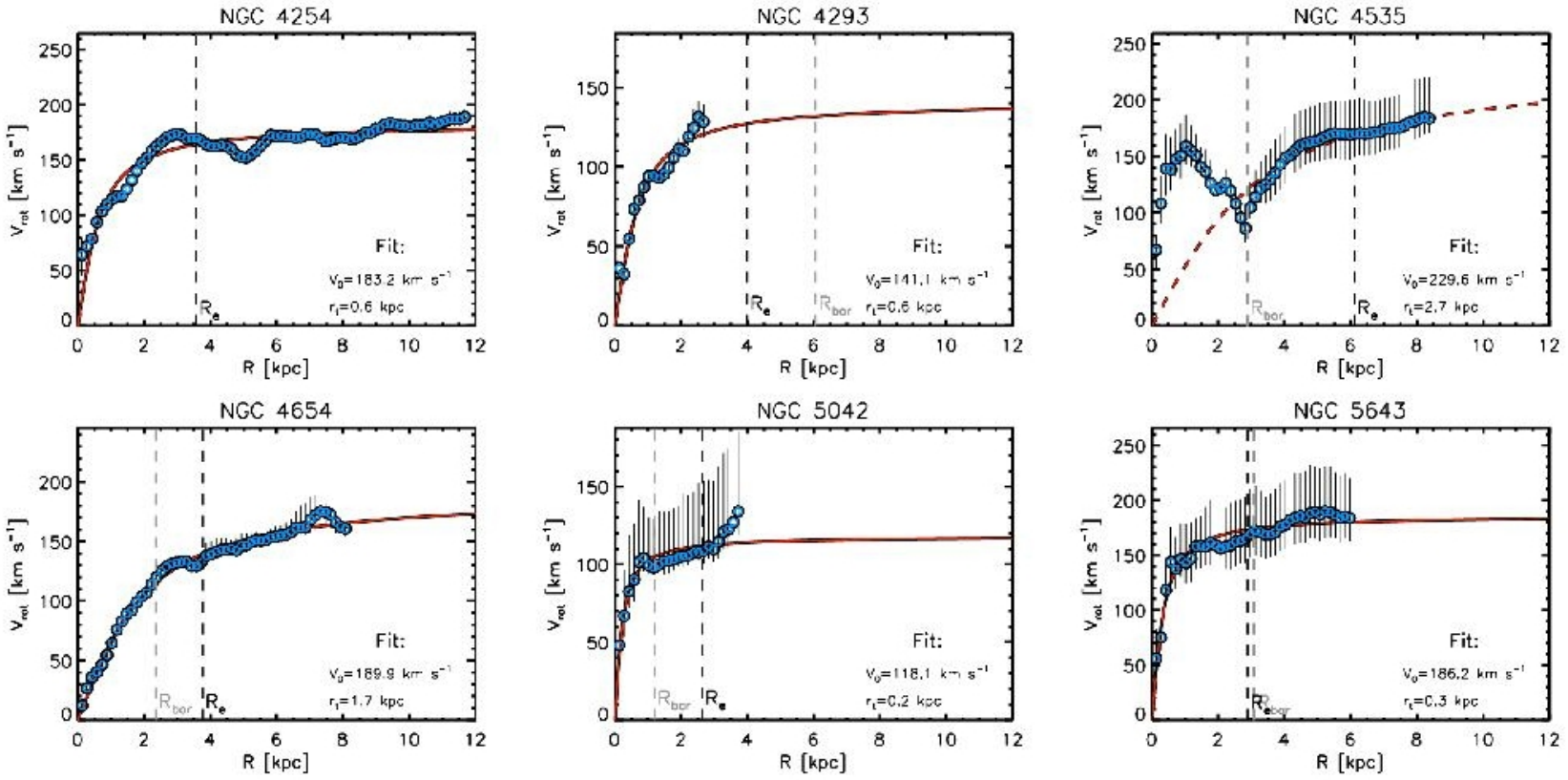

Figure 7. Examples of rotation curves for the subset of galaxies shown in Figure 4 and the Appendix B, sampled at a fixed scale of 150 pc. The errors in $V_{\rm rot}$ mainly stem from uncertainties in our orientation parameters. Smooth fits are shown as red lines, together with their best-fit parameters and the asymptotic velocity V_0. In some panels the red lines are dashed to indicate cases where the central 2 kpc region have been masked before fitting a smooth model. Effective radii and bar lengths are indicated with dashed vertical lines.

Все кривые вращения

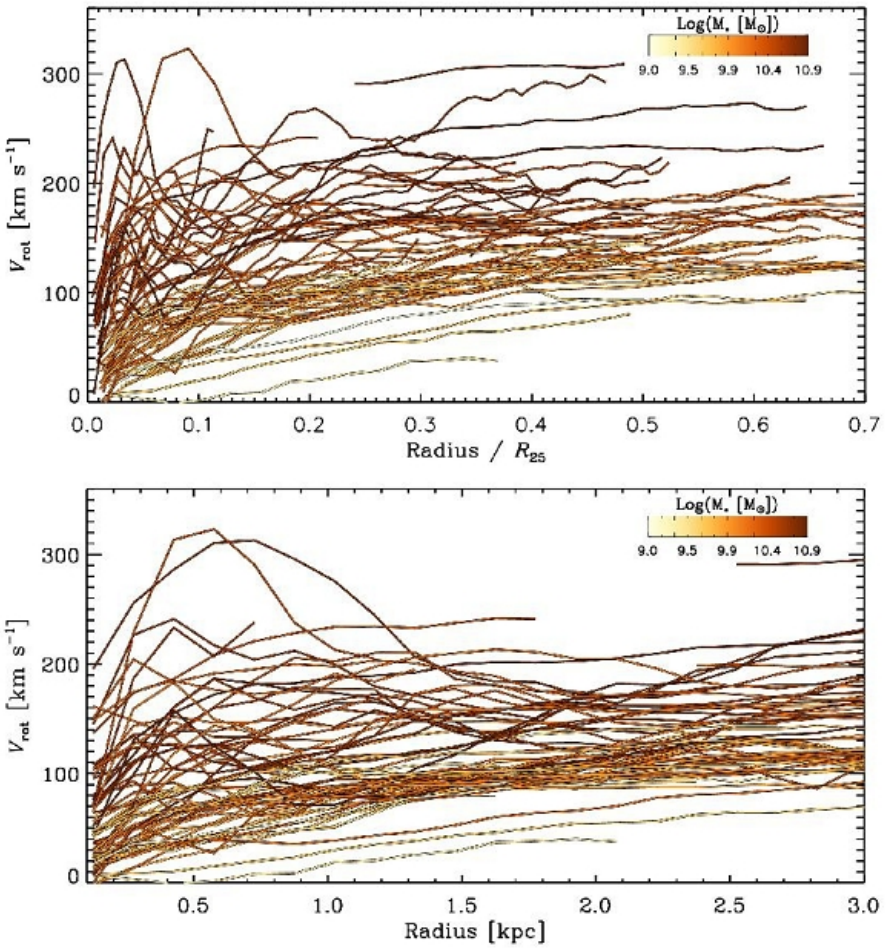

Figure 8. The rotation curves for our sample of 67 galaxies. Top: Radii are normalized by R_{25}. Bottom: Zoom-in on th
3 kpc to highlight the variety of inner rotation curves shapes. The color coding indicates total stellar mass.

minimize fluctuations that most likely arise with non-
circular motions, rather than track variations in the un-

We adopt the empirical parametrization of ro
curves by the function (Courteau 1997):

Всяческие корреляции

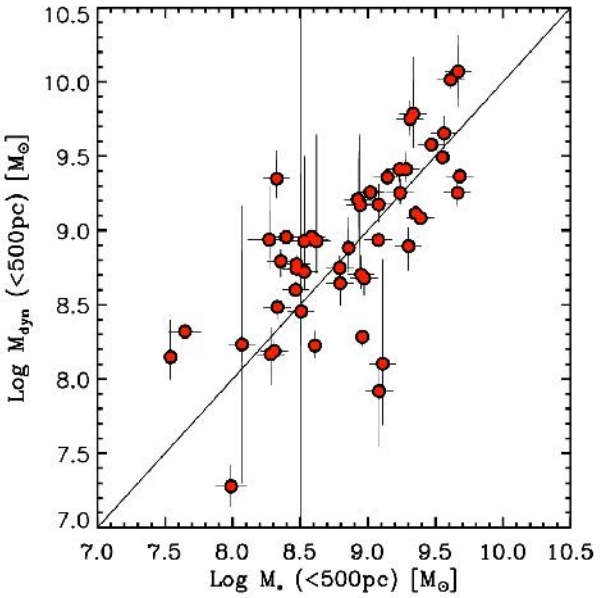

Figure 11. Inner dynamical mass versus stellar mass inside radii ≤ 500 pc. The solid line marks a one-to-one relation. Shown are 51 galaxies that are covered by S^{4}G, excluding galaxies with unconstrained inner rotation curves (NGC 2775, NGC 6744).

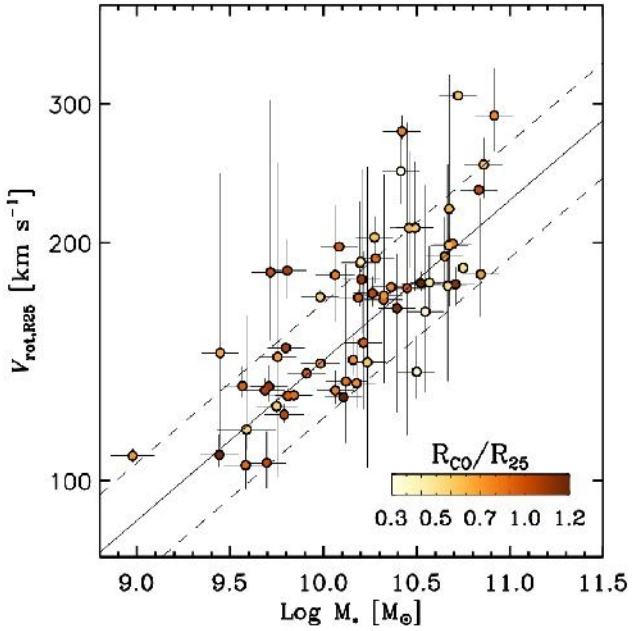

Figure 12. Tully-Fisher relation, based on total stellar masses and outer rotation velocities ($V_{\rm rot,25}$) of our galaxy sample. Rotation velocities are derived from our smooth analytic fits to rotation curves. The color-coding encodes the radial coverage of CO relative to the size of the optical disk. The solid and dashed lines show the stellar Tully-Fisher relation and its scatter from McGaugh & Schombert (2015), respectively. Only systems with robust kinematic fits are

NGC 4535: сильный бар

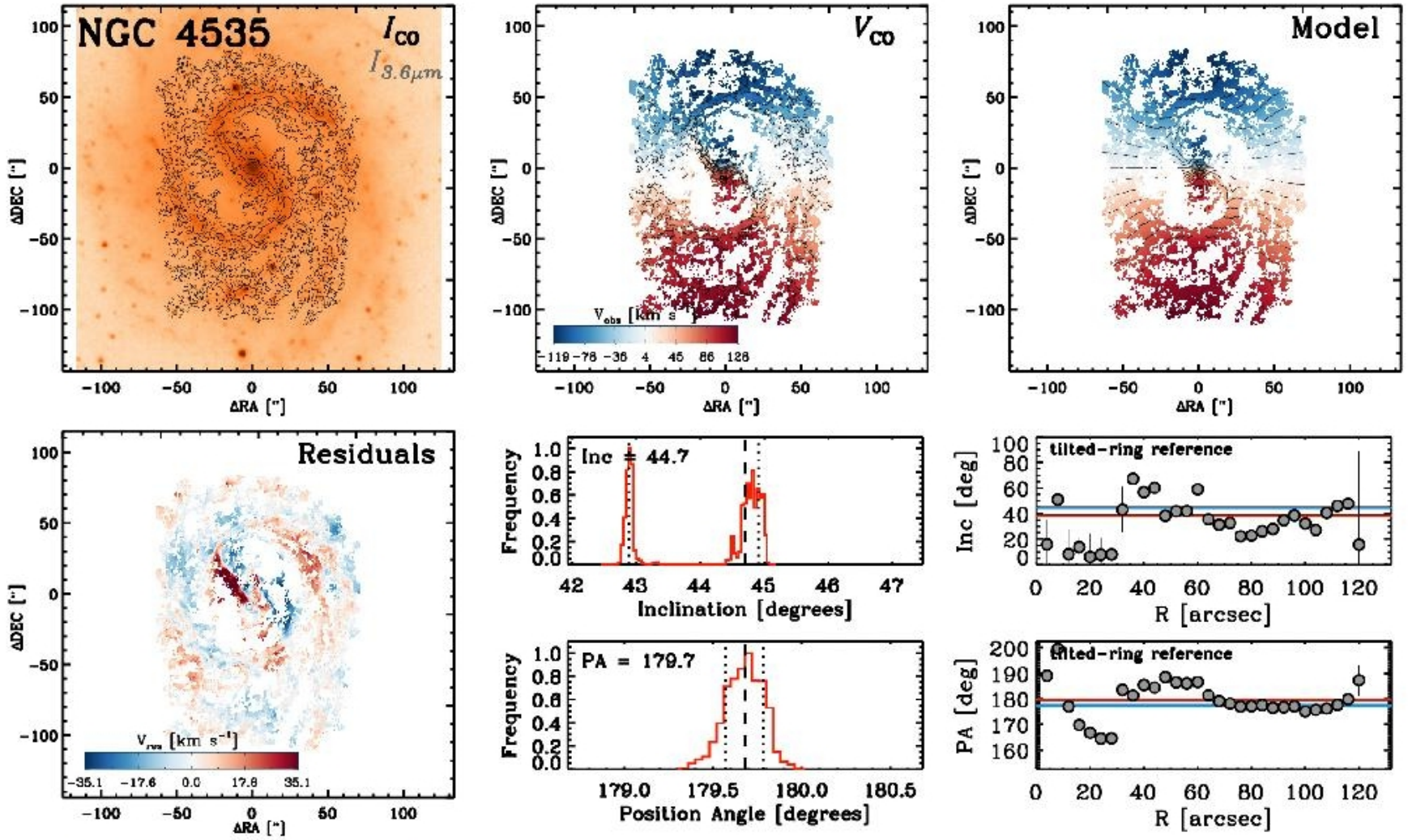

NGC 5643: галактика плашмя

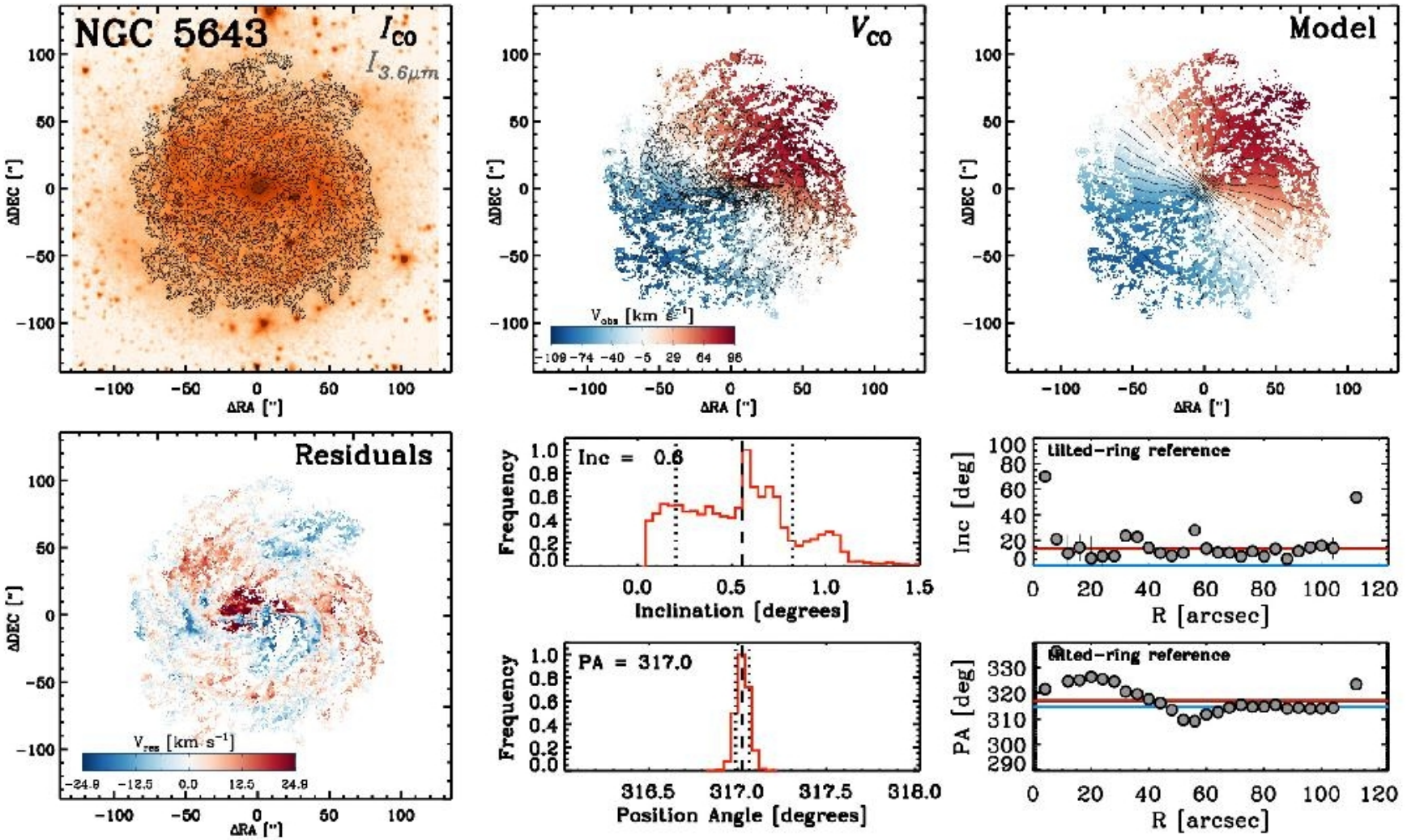

ArXiv: 2006.02009

Deep XMM-Newton Observations of the Most Distant SPT-SZ Galaxy Cluster

Adam B. Mantz,[1,2⋆] Steven W. Allen,[1,2,3] R. Glenn Morris,[1,2,3]
Rebecca E. A. Canning,[1,2] Matthew Bayliss,[4] Lindsey E. Bleem,[5,6]
Benjamin T. Floyd[7], Michael McDonald[8]

[1]*Kavli Institute for Particle Astrophysics and Cosmology, Stanford University, 452 Lomita Mall, Stanford, CA 94305, USA*
[2]*Department of Physics, Stanford University, 382 Via Pueblo Mall, Stanford, CA 94305, USA*
[3]*SLAC National Accelerator Laboratory, 2575 Sand Hill Road, Menlo Park, CA 94025, USA*
[4]*Department of Physics, University of Cincinnati, Cincinnati, OH 45221, USA*
[5]*HEP Division, Argonne National Laboratory, Argonne, IL 60439, USA*
[6]*Kavli Institute for Cosmological Physics, University of Chicago, Chicago, IL 60637, USA*
[7]*Department of Physics and Astronomy, University of Missouri, 5110 Rockhill Road, Kansas City, MO 64110, USA*
[8]*Kavli Institute for Astrophysics and Space Research, Massachusetts Institute of Technology, 77 Massachusetts Avenue, Cambridge, MA 02139, USA*

Submitted 22 April 2020, accepted 1 June 2020.

ABSTRACT

We present results from a 577 ks XMM-*Newton* observation of SPT-CL J0459−4947, the most distant cluster detected in the South Pole Telescope 2500 square degree (SPT-

Вид на скопление в рентгене

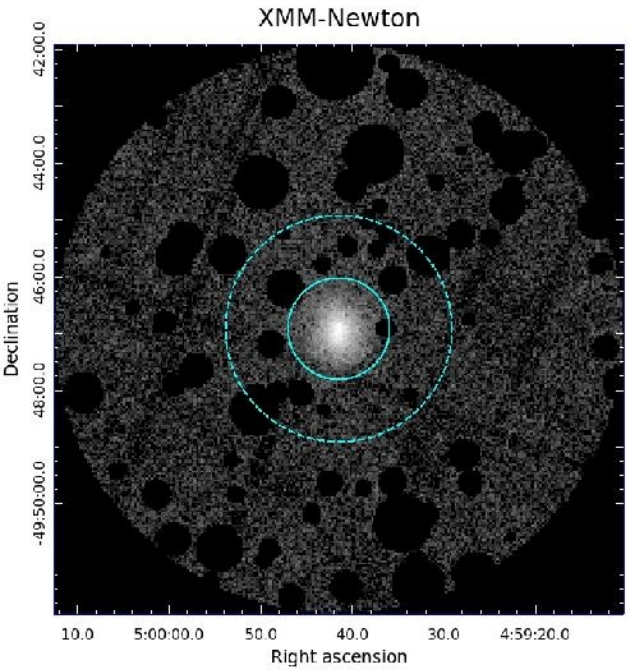

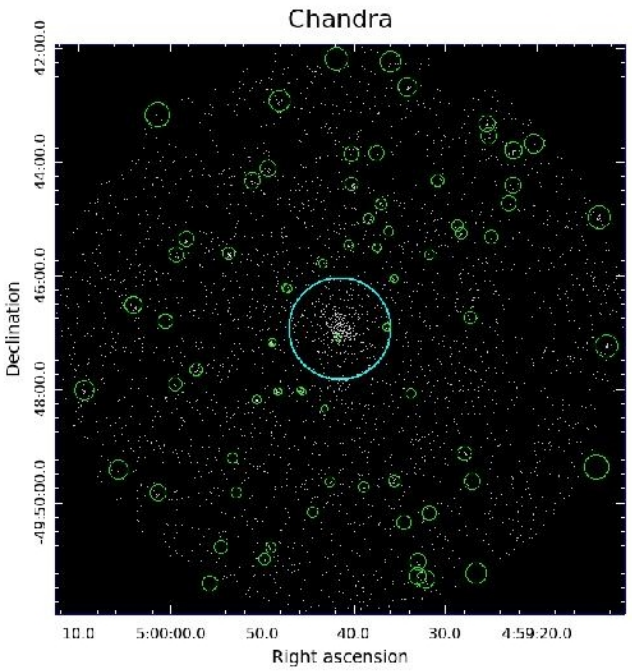

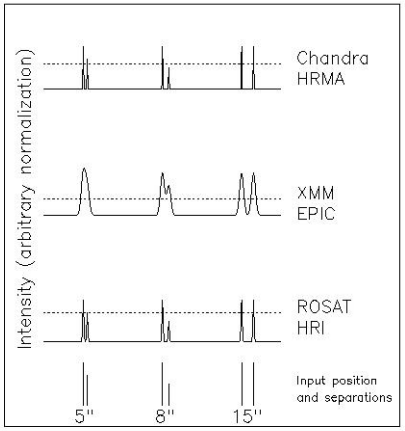

Fig. 1. Typical representation of objects seen by *ROSAT*-HRI, *XMM-Newton*-EPIC and *Chandra*-HRMA. The objects are represented by δ-functions and folded by the corresponding instrumental PSF and efficiency. Full-width-at-half-maximum ($FWHM$) of the on-axis PSFs are $1\farcs7$ for *ROSAT*-HRI, $0\farcs5$ for *Chandra*-HRMA and $6''$ for *XMM-Newton*-EPIC. The dotted line represents schematically the detection limit

Полный рентгеновский спектр

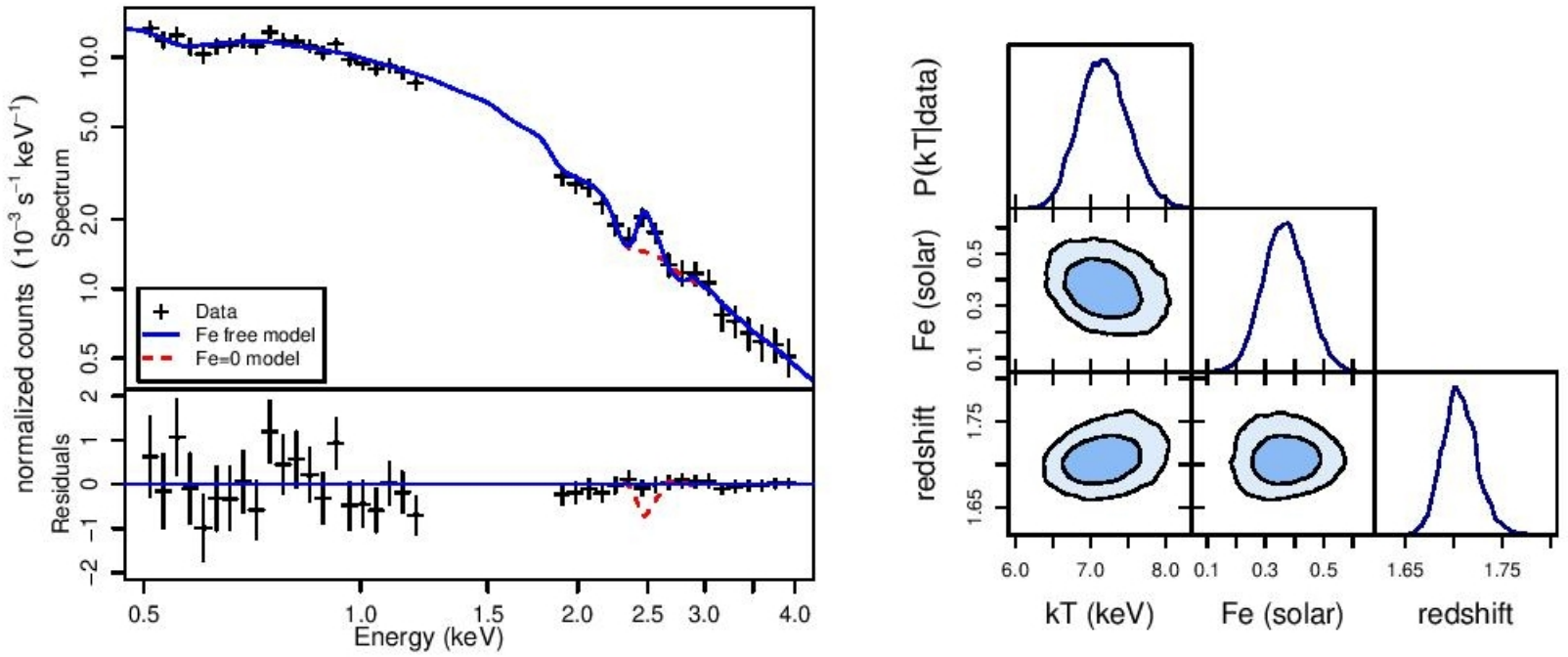

Figure 3. Left: stacked and background-subtracted (for display only) EPIC spectrum of the central arcminute of SPT J0459. Energies in the 1.2–1.9 keV range are excluded due to contamination from instrumental emission lines. The blue, solid curve shows the best-fitting single thermal component model, with a free temperature, metallicity, redshift and normalization. The red, dashed curve shows the best fitting model where the metallicity is fixed to zero, to indicate the strength of the Fe emission feature. The lower panel shows residuals with respect to the model with fitted metallicity. Right: one-dimensional (on-diagonal) and two-dimensional (off-diagonal) marginalized posteriors for the cluster emission model fit to these data.

Найденные параметры газа

4.1 Single spectrum

We first fit XMM spectra extracted from a single circular region of radius $1'$ about the cluster center. While detectable emission from the cluster extends to $\sim 2'$ radius, this smaller region contains > 90 per cent of the total cluster signal; the radius of $1'$ is also conveniently very close to the estimate of $r_{500} \approx 54''$ derived in the next section. From these data, we constrain the "average" properties of the ICM to be $kT = 7.2 \pm 0.3$, $Z/\,Z_{\odot} = 0.37 \pm 0.08$ and $z = 1.705 \pm 0.018$. Our redshift constraint, due to the (rest frame) 6.7 keV Fe emission line complex, is consistent with earlier photometric estimates of 1.7 ± 0.2 (*Spitzer* IR and ground-based NIR data; Bleem et al. 2015) and $1.80^{+0.10}_{-0.19}$ (*Spitzer* and *Hubble*

Table 2. Measured temperatures and metallicities of SPT J0459, marginalized over the cluster redshift in all cases. Shown are results from a single spectrum; two concentric annuli, where mixing of emission from the PSF is accounted for but geometric projection is not; and the same annuli when both the PSF and projection are accounted for. Net (background subtracted) counts are in the 0.5–4.0 keV band. The final column compares the best C statistic with the number of degrees of freedom.

Deprojected	$r^{(1)}_{\rm inner}$ ($''$)	$r^{(1)}_{\rm outer}$ ($''$)	$kT^{(1)}$ (keV)	$Z^{(1)}$ ($Z_{\odot}$)	$r^{(2)}_{\rm inner}$ ($''$)	$r^{(2)}_{\rm outer}$ ($''$)	$kT^{(2)}$ (keV)	$Z^{(2)}$ ($Z_{\odot}$)	Net counts	cstat/dof
No	0	60	7.2 ± 0.3	0.37 ± 0.08	—	—	—	—	11499	4351/5121
No	0	16	8.3 ± 0.7	0.52 ± 0.15	16	120	$6.1^{+0.9}_{-0.7}$	0.29 ± 0.18	12704	8109/8998
Yes	0	16	10.3 ± 2.3	0.69 ± 0.35	16	120	$5.9^{+0.9}_{-0.6}$	0.33 ± 0.17	12704	8109/8998

Разрешаем характеристики вдоль радиуса

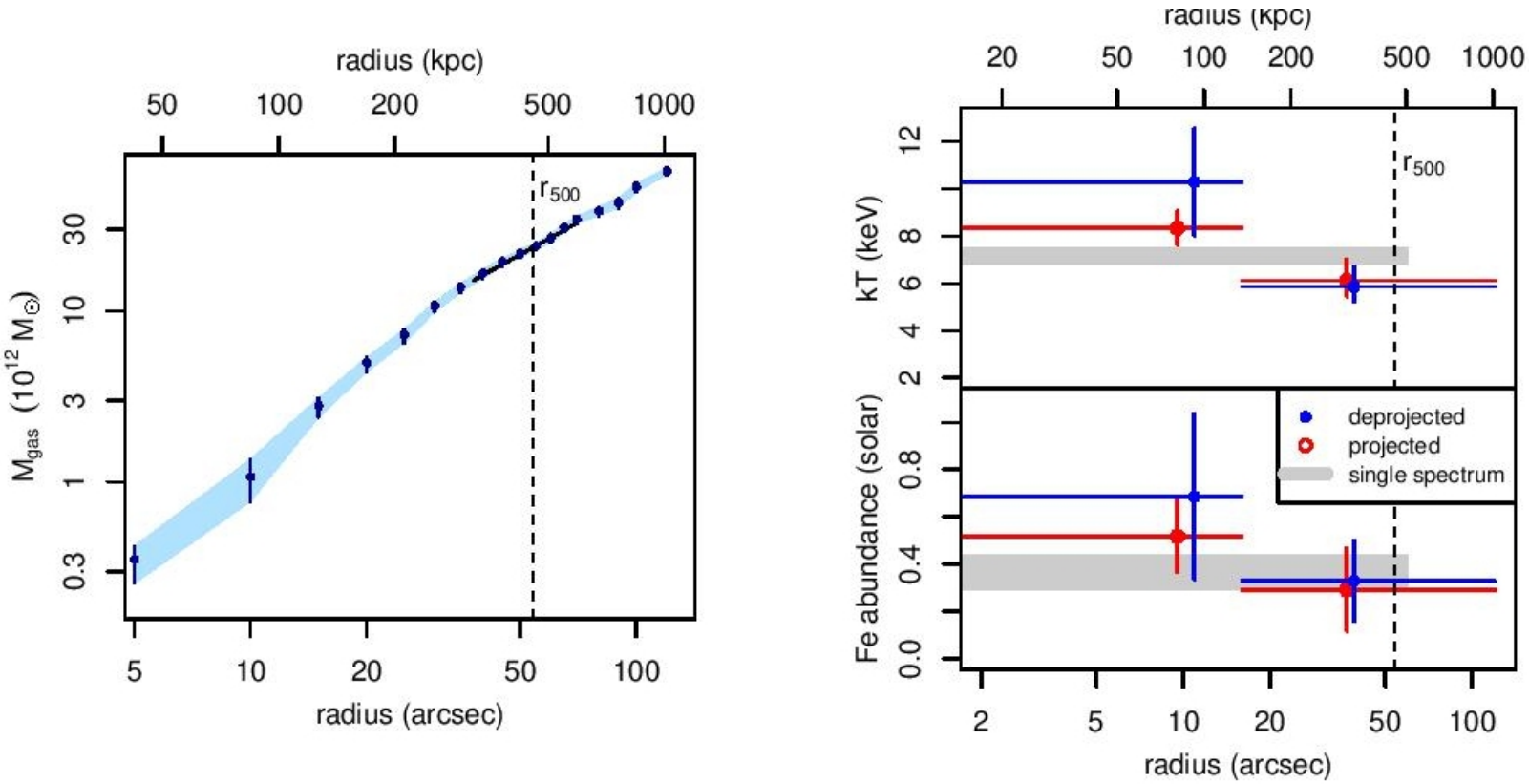

Figure 4. Left: enclosed gas mass profile of SPT J0459 as determined from our analysis in Section 4.2. While the spectral fit leading to this profile marginalizes over cluster redshift, the values of gas mass and radius in physical units shown here assume a cluster redshift of $z = 1.71$. Error bars and shading indicate the 68.3 per cent confidence intervals as a function of radius. The vertical, dashed line shows our estimate of r_{500}, which is insensitive to the assumed redshift within the posterior redshift uncertainty. The solid line shows the typical power-law slope of the gas mas profile at $\sim r_{500}$, 1.25, measured from $z < 0.5$ clusters (Mantz et al. 2016b), with which the measured profile of SPT J0459 agrees well. Right: constraints on temperature and metallicity from the single-spectrum analysis of Section 4.1, as well as the 2-annulus analysis of Section 4.3. Blue points show the results obtained from our standard analysis, accounting for mixing due to both the PSF and geometrical projection (i.e., the values correspond to spherical shells of gas). For comparison, red points show

Нет никакой эволюции!

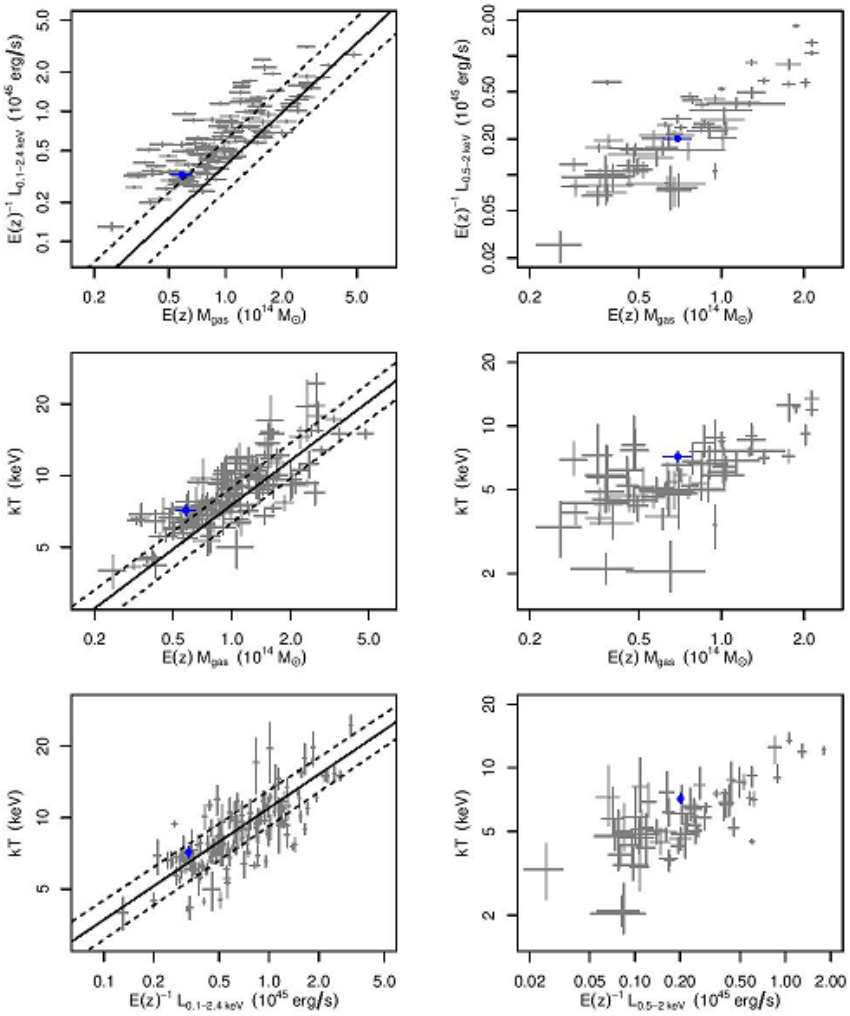

Figure 7. Comparison of the global properties of SPT J0459 (blue point) with lower-redshift cluster samples. Factors of $E(z) = H(z)/H_0$ encode self-similar evolution of the scaling relations. Left column: gray points show measurements from Mantz et al. (2016b, median $z = 0.21$), and solid/dashed lines the corresponding scaling relations (accounting for X-ray flux-selection bias) and their uncertainty (including intrinsic scatter). These measurements were obtained from *Chandra* data, but the procedure for determining each observable (and r_{500}) is essentially the identical to the one used in this work, apart from not needing to model the PSF. Right column: gray points show measurements of 59 SPT clusters observed by XMM (Bulbul et al. 2019, median $z = 0.44$). Here the gas mass of SPT J0459 has been adjusted for consistency with the method used to determine r_{500} for the other SPT clusters.